



Melanoma lesion detection and segmentation using deep region based convolutional neural network and fuzzy C-means clustering

Nudrat Nida^a, Aun Irtaza^b, Ali Javed^c, Muhammad Haroon Yousaf^a,
Muhammad Tariq Mahmood^{d,*}

^a Department of Computer Engineering, University of Engineering & Technology, Taxila, Pakistan

^b Department of Computer Science, University of Engineering & Technology, Taxila, Pakistan

^c Department of Software Engineering, University of Engineering & Technology, Taxila, Pakistan

^d School of Computer Science and Engineering, Korea University of Technology and Education, 1600, Chungjeol-ro, Byeongcheon-myeon, Dongnam-gu, Cheonan-si, Chungcheongnam-do, 31253, Republic of Korea

ARTICLE INFO

Keywords:

Melanoma segmentation
Region proposal
RCNN
Fuzzy C-Means
CAD tool

ABSTRACT

Objective: Melanoma is a dangerous form of the skin cancer responsible for thousands of deaths every year. Early detection of melanoma is possible through visual inspection of pigmented lesions over the skin, treated with simple excision of the cancerous cells. However, due to the limited availability of dermatologists, the visual inspection alone has the limited and variable accuracy that leads the patient to undergo a series of biopsies and complicates the treatment. In this work, a deep learning method is proposed for automated Melanoma region segmentation using dermoscopic images to overcome the challenges of automated Melanoma region segmentation within dermoscopic images.

Materials and methods: A deep region based convolutional neural network (RCNN) precisely detects the multiple affected regions in the form of bounding boxes that simplify localization through Fuzzy C-mean (FCM) clustering. Our method constitutes of three step process: skin refinement, localization of Melanoma region, and finally segmentation of Melanoma. We applied the proposed method on benchmark dataset ISIC-2016 by International Symposium on biomedical images (ISBI) having 900 training and 376 testing Melanoma dermatological images.

Main findings: The performance is evaluated for Melanoma segmentation using various quantitative measures. Our method achieved average values of pixel level specificity (*SP*) as 0.9417, pixel level sensitivity (*SE*) as 0.9781, *F1_s core* as 0.9589, pixel level accuracy (*Ac*) as 0.948. In addition, average dice score (*Di*) of segmentation was recorded as 0.94, which represents good segmentation performance. Moreover, Jaccard coefficient (*Jc*) averaged value on entire testing images was 0.93. Comparative analysis with the state of art methods and the results have demonstrated the superiority of the proposed method.

Conclusion: In contrast with state of the art systems, the RCNN is capable to compute deep features with amen representation of Melanoma, and hence improves the segmentation performance. The RCNN can detect features for multiple skin diseases of the same patient as well as various diseases of different patients with efficient training mechanism. Series of experiments towards Melanoma detection and segmentation validates the effectiveness of our method.

1. Introduction

Melanoma is one of the lethal skin cancer causing death to thousands of people every year. Melanoma usually affects the exposed skin regions i.e. face, neck, arms, and legs that remain on regular basis under the sunlight. Unfortunately, the highest mortality rate amongst the skin

cancers is also associated with the Melanoma. In the USA alone, every year among 87,110 Melanoma cases, 9730 patients lost their lives, that means in every hour one person died due to Melanoma [1]. Similarly, 1150 patients amongst 6800 Melanoma patients died in Canada in 2016 [2]. Melanoma moles have uneven borders and evolving colors i.e. blue, red, brown, black, white and pink representing the severity of the

* Corresponding author.

E-mail addresses: 16F-PHD-CP-53@uettaxila.edu.pk (N. Nida), aun.irtaza@uettaxila.edu.pk (A. Irtaza), ali.javed@uettaxila.edu.pk (A. Javed), haroon.yousaf@uettaxila.edu.pk (M.H. Yousaf), tariq@koreatech.ac.kr (M.T. Mahmood).

<https://doi.org/10.1016/j.ijmedinf.2019.01.005>

Received 4 July 2018; Received in revised form 5 January 2019; Accepted 8 January 2019

1386-5056/ © 2019 Elsevier B.V. All rights reserved.

disease [3]. The moles greater than 6mm in diameter with unusual skin colors need inspection by a dermatologist for possible Melanoma infection. Initially, the dermatologists diagnose Melanoma through visual examination of the skin by measuring the asymmetry, border irregularity, diameter, and color variation of the affected skin [3]. However, due to limited availability of dermatologists earlier Melanoma detection is usually delayed. Moreover, detection of Melanoma at earlier stages reduces the painful series of biopsies and may lead to a permanent cure for the disease. Earlier detection and treatment of Melanoma not only prevents the metastasize of cancerous cell to other organs but also increases the survival rate of patients [4]. To overcome these challenges research is focusing towards the automated detection of melanoma through CAD based solutions [5–8].

In the automated diagnosis of melanoma, handcrafted features were used to distinguish between melanoma affected skin and normal skin [9–12]. However, these features were unable to identify melanoma due to high intra-class variations, i.e., size, color, gel bubbles, clinical rule marks and artifacts, leading to the unsatisfactory performance of CAD systems. To optimize the performance of CAD systems, classification of melanoma is carried out through well defined segmented melanoma area named as region of interest (ROI). It improves the recognition capability, as the affected region provides better representation of Melanoma attributes [13,5,6]. The precise classification of the Melanoma skin regions can occur if the feature extraction steps emphasize only the affected area, as practiced by an expert dermatologist. The foremost reason is that the inclusion of non-affected skin regions with affected skin regions for feature extraction generates weak features, as we are not specifically targeting the ROI. Hence, inaccuracies may be found in classification results. Therefore, the segmentation is considered as a primary step before classification [14–18], to improve the performance of CAD systems.

Traditional segmentation techniques commonly found in literature are used for segmenting Melanoma lesion from normal skin, such as, adaptive thresholding [19], iterative selection thresholding (ISO) [20], Otsu's thresholding [21], level set active contour [22] and statistical region growing [23]. Thresholding based techniques performed good segmentation, when contrast variations are not significant and uniform distribution of chrominance is present within the images. However, in real scenarios, images are occluded with clinical artifacts, and holds illumination and chrominance variations. Therefore, thresholding based techniques unable to segment the Melanoma region accurately. In [23] regions having statistically similar characteristics are split and merged to segment the regions efficiently. However, such methods are unable to perform segmentation on macroscopic images with complex texture and chrominance variations. Therefore, it is a challenging task to segment Melanoma lesion accurately using level set or region growing methods.

Object saliency based detection techniques [24,25] emphasize on detection of skin lesion and consequently, result in better segmentation of Melanoma regions. In [24], super-pixels based hyper-graph modeling is used to capture the saliency contextual information for melanoma segmentation. In [26], Laplacian sparse super-pixels based approach captures the contextual information and generates a model to segment the Melanoma lesion. However, all these automatic and semiautomatic

segmentation techniques use low-level color and texture information that are unable to represent wide variations of Melanoma in poor contrast and difficult boundaries lesion.

Recently, deep learning have improved the performance records in medical analysis applications [27–32]. Deep convolutional neural networks (CNN) use small image patches of Melanoma for training and perform region segmentation in the test images based on the trained model. Like other fields, CNN's significantly improve recognition ability of Melanoma using deep convolutional features [33]. Almost all deep learning CNN models rely on preprocessing of input images to overcome the problem of feature map saturation [34]. Therefore, in [35], SegNet based networks apply batch normalization to skip the preprocessing of input images. SegNet maps the input image pixels into semantical labels through feature learning. In [34], a hybrid deep learning approach based on CNN and recurrent neural network (RNN) was employed for Melanoma region segmentation without any preprocessing step. In [36], fully convolutional network (FCN) was applied for Melanoma detection in semi-automatic fashion.

In this paper, we propose a method for Melanoma lesion detection and segmentation based on deep regional convolutional neural network (RCNN) and Fuzzy C-mean (FCM) clustering. The RCNN resolves the insufficient samples problem through unsupervised pre-training and supervised fine-tuning regions for localization of the objects [37]. At test time, RCNN generates several category-independent region proposals for image queries, and extracts a fixed-length feature vector from each proposal using a CNN; afterward, classifies each region with higher precision. Once the affected regions are detected, FCM precisely extracts the affected patches with variable boundaries that can be used for recognition of the disease.

2. Proposed methodology

2.1. System overview

The segmentation of Melanoma is a challenging task due to wide variations in appearance, size, texture, color, and shape of the Melanoma regions; whereas, the presence of the hair and tiny blood vessels also complicate Melanoma detection and segmentation. Meanwhile, image acquisition artifacts like illumination conditions, contrast variations and clinical artifacts such as ruler scale marks, gel bubbles, color swatches also serve as barriers in precise segmentation. Few sample images are shown in Fig. 1 from ISIC 2016 dataset with different artifacts. Therefore, Melanoma detection method must be robust against these challenges. In our proposed approach, the tiny blood vessels, and hair are removed through the morphological closing operation. The resultant image becomes smooth that is further enhanced by using the un-sharp filter [38]. The artifacts are automatically fixed once the RCNN is applied over the resultant image. The foremost reason is that the trained RCNN only consider the Melanoma regions as a ROI and remaining image portions are labeled as background. For RCNN training, the ground truth images are binarized and region-labeling segmentation [39] is applied to extract the largest connected component coordinates for Melanoma indication. The RCNN then learns a model to detect Melanoma-regions through regression layer and

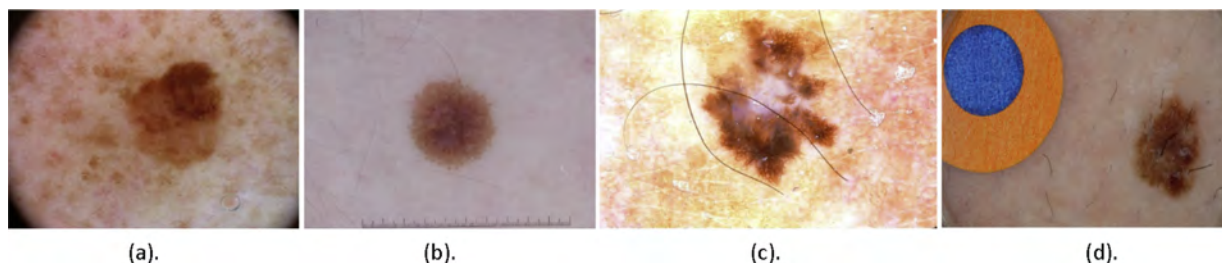


Fig. 1. Artifacts within ISIC 2016 skin images. (a) Illumination variation. (b) Clinical scale marker. (c) Skin hair. (d) Clinical color swatches.

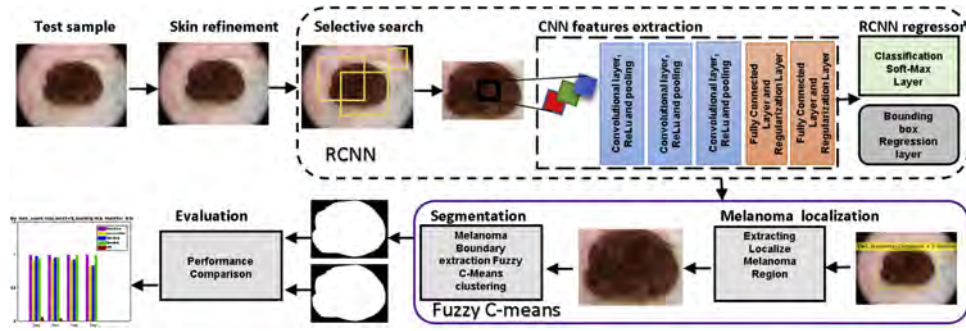


Fig. 2. Proposed framework for localization and segmentation of Melanoma lesion.

selective search [40]. The trained model is then applied over the test images that localizes the Melanoma regions along with regression-confidence score. The regions where regression-confidence score is greater than 0.5 are considered for segmentation step through FCM clustering algorithm. The architecture of the proposed method is provided in Fig. 2.

2.2. Skin refinement

For a given input color image $I(x, y)$ the morphological closing operation removes the hair from skin through line structuring elements S_1 . The closing operation performs dilation \oplus and then erosion \ominus on RGB image with line structuring element, as described:

$$I_{mor}(x, y) = (I(x, y) \oplus S_1) \ominus S_2 \quad (1)$$

Where, the S_1 and S_2 consists of 10 pixels in direction of 90° and 180° against every pixel and $I_{mor}(x, y)$ is the resultant morphed image. The reason behind the application of two different structuring elements for two consecutive closing morphological operations is to eliminate thick and thin hairs. The resultant image is free from hair and blood vessels artifact with slight blurring effect due to the morphological closing operations. In order to remove the blurring effect we apply the un-sharp filter $\varpi(x, y)$ over $I_{mor}(x, y)$ to obtain the un-sharp image $I_b(x, y)$ as,

$$I_b(x, y) = I_{mor}(x, y) \times \varpi(x, y) \quad (2)$$

where

$$\varpi(x, y) = -\frac{1}{\pi\sigma^4} \left[1 - \frac{x^2 + y^2}{2\sigma^2} \right] e^{-\frac{x^2 + y^2}{2\sigma^2}} \quad (3)$$

The obtained un-sharped image $I_b(x, y)$ is then subtracted from the $I(x, y)$ to obtain the sharpened image $I_s(x, y)$ as described:

$$I_s(x, y) = I_{mor}(x, y) + (I_{mor}(x, y) - I_b(x, y)) \quad (4)$$

The resultant image $I_s(x, y)$ is free from hair and blood-vessel artifacts at the same time preserving the precise details for Melanoma detection.

2.3. Melanoma detection and localization using RCNN

The RCNN generates m region proposals against the input image $I_s(x, y)$. RCNN's soft-max layer [37] generates the prediction confidence score to classify each region proposal as normal or abnormal (i.e. Melanoma affected) skin patch. Afterwards, the greedy suppression algorithm [40] is applied on to exhaustively search the melanoma regions and generate the bounding box over the area as $PI(x, y, w, h)$; where, the bounded area PI is centered at (x, y) coordinates and w, h represent the width and height of the bounding box.

In our approach, the RCNN training phase includes both the detected and ground-truth regions in the form of training pairs. The training pairs can be represented as: $\{(PI^i, GI^i)\}_{i=1, \dots, N}$, where i represents the index of N training samples and GI^i are the ground-truth regions. The GI can be represented as: $GI(x, y, w, h)$ with similar

definitions of x, y and w, h as of the PI . For convenience of explanation in remaining equations we have dropped superscript i from the training pairs.

2.3.1. Feature extraction

Traditional object detection techniques like viola Jones [41] and histogram of gradients (HOG) [42] imply sliding window to localize the object of interest i.e. people, cars, faces etc. However, the breakthroughs of deep learning techniques i.e. CNN replaced the earlier detection algorithms with good accuracy. However, the CNN based object detection methods are computationally extensive as they follow the similar sliding window approach for object detection. Therefore, RCNN introduced selective search algorithm to improve the efficiency of the CNN by feeding reduced number of region proposals. Then, down sample the regions to overcome shape and spatial associations and detect the objects at various aspect ratios and different pyramid levels [40], at the same time preserving the precise details for Melanoma detection.

Melanoma-affected regions vary in shape and location, and to precisely model these variations image pyramids of RCNN acquire deep feature representation to detect disease. The image pyramid $PI_j(x, y, w, h)$ represents the image $I_s(x, y)$ through repeated smoothing and down-sampling, and the subscript $j = \{1, 2, \dots, 4\}$ represents various levels of the image pyramid. The whole process of smoothing and down-sampling can be represented as:

$$PI_j(x, y) = I_s(x, y) - 4 \sum_{m=-2}^2 \sum_{n=-2}^2 \varpi(m, n) I_s\left(\frac{x-m}{2}, \frac{y-n}{2}\right) \quad (5)$$

For precise modeling the melanoma characteristics, the selective search step of RCNN captures texture, color, and intensity of melanoma regions through multiple layers (Table 1). Each layer is a local representation of probable melanoma. Three hyper-parameters of RCNN

Table 1
The RCNN architecture.

sr.no.	Layers	Filter	Size	Stride	Padding
1	Input Layer		$32 \times 32 \times 3$		
2	Convolution layer	3	5×5		0
3	Maximum pooling		3×3	2	0
4	RELU				
5	Convolution layer	32	5×5	1	2
6	RELU				
7	Average pooling		3×3	2	0
8	Convolution layer	64	5×5	1	2
9	RELU				
10	Average pooling		3×3	2	0
11	Fully connected	64			
12	RELU				
13	Fully connected	2			
14	Softmax classification				
15	Regression				

Table 2
Spatial output volume size of RCNN layers. Fully connected layer Fc5 representing two class distribution of Melanoma and normal skin region.

Layers	Input	Filter	# filter	Output
Convolutional Layer 1	32 × 32 × 3	5 × 5	3	27 × 27 × 3
Convolutional Layer 2	27 × 27 × 3	5 × 5	32	12 × 12 × 32
Convolutional Layer 3	12 × 12 × 32	5 × 5	64	5 × 5 × 64
Fully Connected Layer 4	5 × 5 × 64		64	64
Fully Connected Layer 5	64		2	2

architecture the number and arrangement of output feature volume (Table 2).

2.3.2. Regression

Regression step is applied for precise localization of Melanoma regions. Selective search step generates the region and assign a confidence score to each proposal. The regressor utilize CNN features to predict the Melanoma region and introduced the bounding box across the affected area. Optimal transformation functions are used to reduce the detection error and map the predicted bounding box PI to the ground truth bounding box GI . The four transformation functions $b_x(PI)$, $b_y(PI)$, $b_w(PI)$, and $b_h(PI)$ were used for mapping predicted region against the ground truth as:

$$GI_x = PI_w b_x(PI) + PI_x \tag{6}$$

$$GI_y = PI_h b_y(PI) + PI_y \tag{7}$$

$$GI_w = PI_w \exp^{b_w(PI)} \tag{8}$$

$$GI_h = PI_h \exp^{b_h(PI)} \tag{9}$$

where

$$b_*(PI) = w_*^T \phi_3(PI) \tag{10}$$

The $b_x(PI)$, and $b_y(PI)$, specify the scale invariant mapping of centroid of PI , whereas, $b_w(PI)$, and $b_h(PI)$ represents the log space mapping of width and height of PI . After learning optimal transformation maps, the input region proposals were transformed into the predicted ground truth Melanoma regions. The transformation functions $b_x(PI)$, $b_y(PI)$, $b_w(PI)$, and $b_h(PI)$ linearly map the third pooling layer features of predicted region proposal PI , denoted by $\phi_3(PI)$ (Eq. (10)). Whereas, b_* is one of the transformation function and w_* represents the weight parameters (adapted through gradient decent algorithm for weight optimization) for precise detection of Melanoma affected regions.

In the proposed algorithm for training pairs (PI, GI) , regression targets are denoted as R_* , numerically specified as follows:

$$R_x = \frac{(GI_x - PI_x)}{PI_w} \tag{11}$$

$$R_y = \frac{(GI_y - PI_y)}{PI_h} \tag{12}$$

$$R_w = \log\left(\frac{GI_w}{PI_w}\right) \tag{13}$$

$$R_h = \log\left(\frac{GI_h}{PI_h}\right) \tag{14}$$

The information extracted from proposal PI improves learning, if PI is *nearby* one of the ground-truth boxes GI [37]. In our implementation “nearness” was obtained by assigning the PI to the ground-truth GI when intersection over union (*IoU*) score is greater than 0.5. Remaining lower scores were rejected by the algorithm.

2.3.3. Training parameters for RCNN

To fine-tune the RCNN for precise classification and localization of

Melanoma, auxiliary labeled-dataset CIFAR10 [43] as a pre-classification step for transfer learning is used. On achieving state-of-the-art operational accuracy on the CIFAR10 dataset, RCNN was tuned to perform Melanoma classification through transfer learning [44]. For Melanoma localization, we used wrapped region proposals along with ground truth labels for network training.

To reduce the classification error for Melanoma, the stochastic gradient descent algorithm is used for the optimization of the weights. For training, we used mini-batch size ζ of 128, learning rate α of 0.001, and learning drop factor β of 0.1 after detailed experimentation. The piecewise learning schedule automatically adjust learning rate during the training phase. To reduce localization error, 500 epochs were chosen to optimize the cost function. In this way, training of RCNN is repeated 500 times for better localization of melanoma

2.3.4. Melanoma detection at test time

For testing images, selective search was applied to extract the region proposals that were wrapped to make the regions compatible for presenting to the input layer of CNN. We have used softmax cross entropy probabilities to identify the Melanoma affected region. The deep convolutional feature vectors fed into sotmax layer to compute confidence scores. All the scored proposal within an image obtained from CNN were used to accept the region having higher threshold intersection over union (*IoU*) overlap for precise localization.

2.4. Melanoma segmentation using fuzzy C means (FCM)

RCNN localize the affected Melanoma region, to reduce the search space for precise segmentation of affected region boundaries. The localize Melanoma area was cropped using the computed coordinates $R(x, y, w, h)$, to determine the accurate boundary of affected region. To estimate the boundary of affected area from healthy skin, we opt FCM clustering to group pixels into healthy and Melanoma region [45].

FCM clustering based on optimization of objective function J_d , to refine the segmentation of cluster $c_a \in \{1, 2\}$, under defined initial conditions. Where d is total number of pixels of $R(x, y, w, h)$ in RGB color space, S_{sa} is degree of membership of pixel within cluster a , and c_a is center of cluster. The fuzzy clustering partition $R(x, y, w, h)$ in optimize iterative fashion, to reduce the distance by updating the membership S_{sa} of $R(x, y, w, h)$ with associated clusters c_a . To represent clusters, pixels of $R(x, y, w, h)$ are generalized by computing J_d within the group as sum of square error (Eq. (17)) to find the local minima. For simplicity we will denote $R(x, y, w, h)$ as R in following mathematical expressions (Eqs. (15)–(17)).

$$S_{sa} = \frac{1}{\sum_{k=1}^{24} \frac{\|R - c_a\|^{\frac{2}{d-1}}}{\|R - c_k\|}} \tag{15}$$

$$c_a = \frac{\sum_{s=1}^N S_{sa} R}{\sum_{s=1}^N S_{sa}^d} \tag{16}$$

$$J_d = \sum_{s=1}^d \sum_{a=1}^2 S_{sa}^d \|R - c_a\|^2 \tag{17}$$

Initial terminating criteria γ was defined between 0 and 1. To terminate the iteration γ a threshold was selected greater than $\max_a |S_{sa}^{k+1} - S_{sa}^k| < \gamma$, where k is number of iteration to update the cluster center c_a for reevaluating the computed probabilities of association within c_a . In our case, FCM requires $k = 24$ as maximum number of iterations to segment the Melanoma lesion. Finally, on convergence of cluster centroid terminates the algorithm, resulting in clusters of affected and non-affected region.

3. Results and experiments

3.1. Dataset

The performance of proposed framework was evaluated on benchmark dataset ISIC 2016 by “International Symposium on biomedical images(ISBI) in the challenge of Skin lesion analysis towards Melanoma detection” [46]. The dataset for segmentation comprised of 900 training and 380 test Melanoma images. To validate the results of segmentation and classification the ground truth images were provided along with the dataset and were compiled by a panel of the dermatologists.

Moreover, we have tuned our RCNN on CIFAR-10 [43] for precise localization of Melanoma. On achieving state-of-the-art operational accuracy on the CIFAR10 dataset, RCNN was tuned to perform Melanoma classification through transfer learning approach. The CIFAR-10 dataset constitute of 32×32 resolution RGB 60,000 images for ten classes. On average, there are 6000 samples per class.

3.2. Evaluation metrics

In this section we are presenting evaluation metrics for validation of each phase of the proposed system.

3.2.1. Skin refinement

To evaluate the skin refinement phase we have used mean squared error (MSE), root mean squared error (RMSE), signal to noise ratio (SNR), peak signal to noise ratio (PSNR), and universal image quality index (UIQI).

MSE is the average difference between skin refined image $I_s(x, y)$ and input noisy image $I(x, y)$ whereas, RMSE is the square root of MES. MSE and RMSE is computed using following equations:

$$MSE = \frac{1}{mn} \sum_{i=0}^{m-1} \sum_{j=0}^{n-1} [I_s(i, j) - I(i, j)]^2 \quad (18)$$

$$RMSE = \sqrt{\frac{1}{mn} \sum_{i=0}^{m-1} \sum_{j=0}^{n-1} [I_s(i, j) - I(i, j)]^2} \quad (19)$$

For robust image enhancement the values of MSE and RMSE should be minimum.

The signal to noise ratio (SNR), and peak signal to noise ratio (PSNR) as in (Eq. (20, 21)), are the widely used measures to determine the quality of the image. The higher values of SNR, and PSNR indicates the image enhancement quality. For good image enhancement, the empirical value of PSNR should be greater than 20 db [47]. The SNR, and PSNR can be computed as:

$$SNR = 10 \times \log_{10} \left(\frac{P_{I_s}}{P_I} \right) \quad (20)$$

$$PSNR = -20 \times \log_{10} \left(\frac{I_s(\max)}{MSE} \right) \quad (21)$$

UIQI estimates the linear correlation of input image and skin refined image in terms of structure, contrast and luminance information during the skin refinement phase. The UIQI can be computed as follows:

$$UIQI = \frac{4\sigma_{I_s I} \bar{I}_s \bar{I}}{(\sigma_s^2 + \sigma_I^2) [\bar{I}_s^2 + \bar{I}^2]} \quad (22)$$

In Eq. (22) σ , \bar{I}_s , and \bar{I} represents the variance, standard deviation, and mean of skin refined image and mean of input image respectively. The UIQI value range is between -1 to 1 that further confirms the quality of image after the image enhancement [48]. It is notable from Table 6, that skin refinement phase successfully remove some artifacts like hair, and refine the image from clinical and natural artifact (e.g. black frame, clinical ruler marks, clinical color swatches).

3.2.2. Melanoma localization

RCNN performs Melanoma region detection using greedy overlapping criteria of ground truth box and predicted box, known as intersection-over-union (IoU), as shown in Eq. (23). Melanoma area detection acceptable range of IoU is 0.5–1, where 0.3–0 for background normal skin region. The correctly predicted box is known as true positive, otherwise as false positive, as follows:

$$IoU = 2 * \frac{TP}{TP + FN + FP} \quad (23)$$

For evaluation of localization phase, we have used mean average precision (mAP) to compute the average precision to detect melanoma region, as shown below:

$$mAP = \text{mean} \frac{TP}{TP + FP} \quad (24)$$

3.2.3. Melanoma segmentation

For performance evaluation of segmentation phase, we have considered the dice score (Di), Jaccard coefficient (Jc), pixel level specificity (SP), pixel level sensitivity (SE), and pixel level accuracy (Ac) as the evaluation measures. These are the evaluation criteria that were also used in the ISBI challenge for validating the quality of segmentation.

$$Di = 2 * \frac{2 * TP}{FN + (2 * TP) + FP} \quad (25)$$

$$Jc = 2 * \frac{TP}{TP + FN + FP} \quad (26)$$

$$SP = \frac{TP}{TP + FP} \quad (27)$$

$$SE = \frac{TP}{TP + FN} \quad (28)$$

$$Ac = \frac{TP + TN}{TP + FP + FN + TN} \quad (29)$$

Where TP, TN, FP, and FN represents the number of true positive pixels, true negative pixels, false positive pixels, and false negative pixels, respectively. A Melanoma region pixel is considered as true positive if it is detected as Melanoma; otherwise it is referred as false negative pixel. A normal skin pixel is considered as true negative pixel if it is detected as normal skin pixel; otherwise it is referred as false positive pixel. To analyze the segmentation performance compared with the state of the art system we have plotted the receiver operating characteristic (ROC) using recorded values of sensitivity and specificity.

3.3. Results and discussion

In this section, we will discuss the results obtained at each step of the Melanoma detection through the proposed algorithm.

3.3.1. Skin refinement

At skin refinement phase, noisy artifacts were removed to enhance the visual information and improve the segmentation of affected regions. From the results presented in Fig. 3, we can observe that the image after skin refinement phase is free from various artifacts i.e. hair, blood vessels, and clinical rule marks etc. To estimate the quality of image we have computed the image quality parameters such as RMSE, PSNR, and UIQI, and results are represented in Table 3. From the results we can observe that values of PSNR are higher than 20 db that represents higher information rate in the refined images. Similarly, UIQI represents fine resemblance ratio of skin refined image and input noisy image in terms of structure, and contrast within the input image.

From Table 3, it can be observe that the highest value of PSNR is 37.78 at minimum RMSE error. Higher the PSNR value smaller will be the RMSE. Similarly, lowest PSNR value is 18.90 at the cost of largest

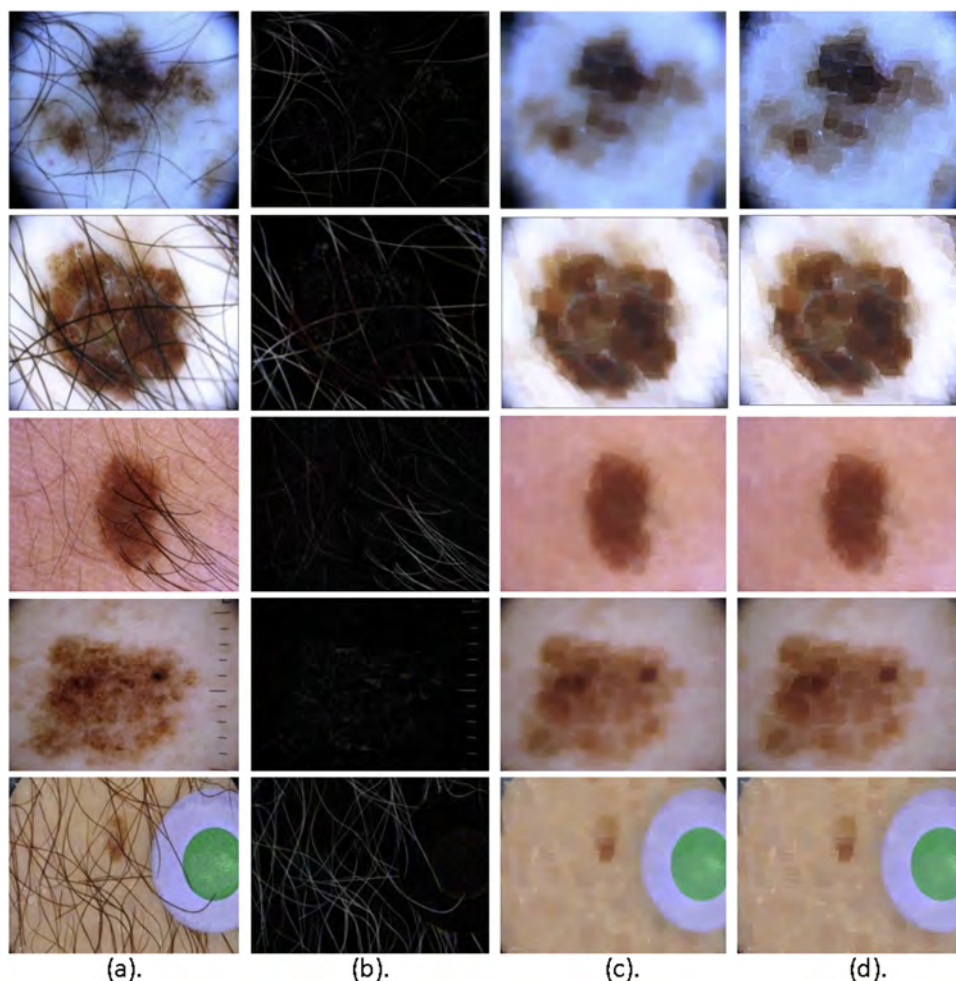


Fig. 3. Skin refinement phase: (a) Input image with artifacts i.e. black frame, thick and thin hair, gel bubbles, clinical ruler marks, color swatches, etc. (b) Outcome of the closing morphological operation for artifacts removal. (c) Resultant smooth image. (d) Sharp image after convolution of un-sharped filter.

Table 3
Skin refinement performance measures computed for 20 test images with noisy artifacts. PSNR, UIQI, and RMSE is recorded for each type of artifact to estimate the strength of skin refinement phase of proposed framework.

Image artifacts	PSNR	UIQI	RMSE
Black frame	33.00	0.61	9.98
	28.52	0.41	16.56
	34.00	0.60	9.24
	30.30	0.54	13.50
Thick hair	30.67	0.60	12.92
	31.75	0.50	11.41
	30.02	0.50	13.93
	35.70	0.51	7.25
Thin hair	34.50	0.43	8.31
	32.57	0.64	10.39
	33.70	0.58	9.15
	37.78	0.56	5.69
Scale marks	18.90	0.40	50.12
	29.71	0.57	14.43
	32.26	0.55	10.77
	32.35	0.50	10.65
Color swatches	35.31	0.55	7.57
	32.35	0.53	10.66
	33.05	0.67	9.82
	30.15	0.70	13.72

RMSE of 50. Images having *PSNR* value approximately equal to 33 represents the *RMSE* of 9. *PSNR* value portray the strength of information within the skin-refined image, greater values of *PSNR* indicates higher rate of information within an image. The value of *RMSE* represents the loss of energy in enhanced image without considering the perceptual quality of image. *RMSE* calculates the intensity difference between input and skin refined image, lower value represents fewer pixels distortion in enhanced image [47].

UIQI measures the quality of image in accordance with human visual system using luminance, contrast and structural information so, its value is not dependent upon value of *PSNR*, *SNR* and *RMSE*. The largest value of *UIQI* is 0.7 that represents minor loss of information in terms of contrast, luminance and structural information at *PSNR* value of 30. It is notable that the range of *UIQI* of 20 test skin-refined images are within acceptable human visual perceptible range (0.4–0.7). Therefore, it is deduced the skin refinement phase remove artifacts and sharpen image without degrading the quality of image.

3.3.2. Melanoma localization

Localization is the next step in proposed RCNN based Melanoma detection. The visual representation of feature map generated through soft-max layer of RCNN to classify the affected regions are shown in Fig. 4. RCNN precisely distinguishes the affected regions in the test images, as shown in Fig. 4. The receptive fields extracted from convolutional layers assigns different probabilities to the Melanoma region

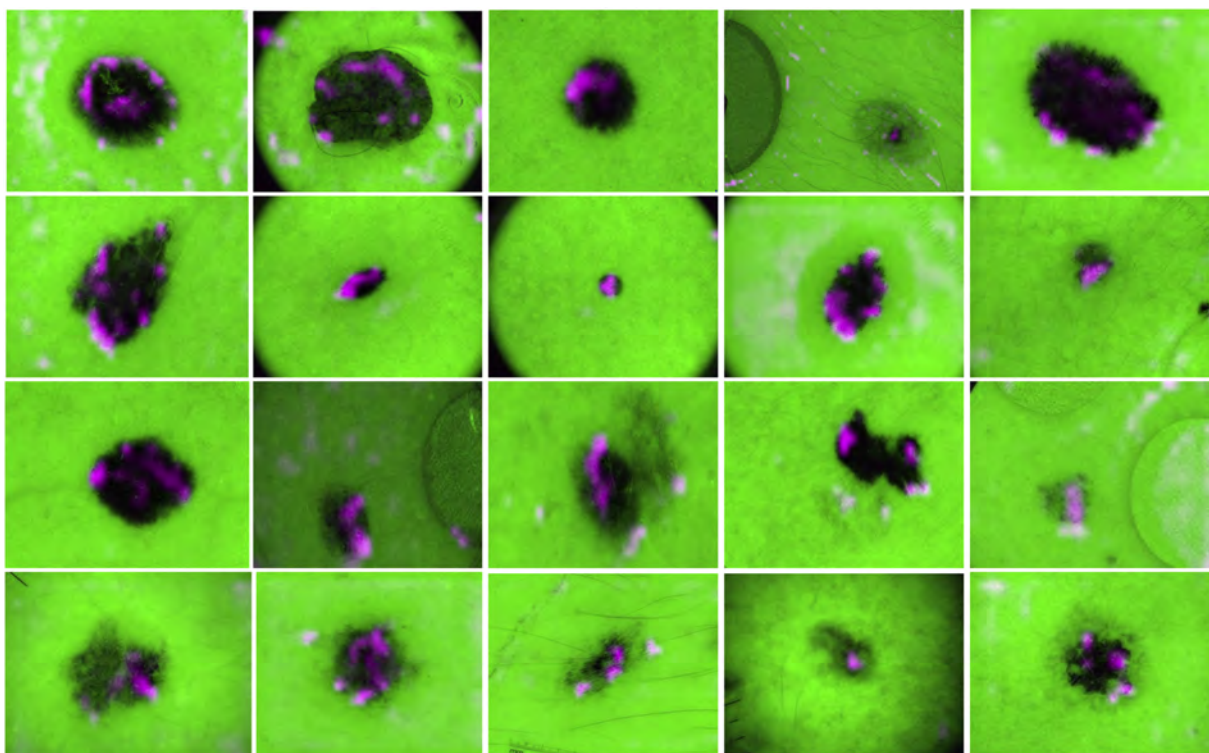


Fig. 4. Visual representation of feature map generated by RCNN soft-max layer for 20 test images to classify Melanoma and normal skin region.

Table 4
mAP score to localize Melanoma using RCNN

Image	Image 1	Image 2	Image 3	Image 4	Image 5	Image 6	Image 7	Image 8	mAP
Precision	0.98	0.87	0.93	0.97	0.99	0.89	0.95	0.84	0.93

and the remaining normal skin region along with some clinical artifacts for the localization of Melanoma area. The RCNN (Table 2) extract convolutional features from the region proposals generated from the selective search and then map them in accordance with the CNN trained model to classify the region proposal. To train a binary classifier for

Melanoma localization, the region enclosing Melanoma affected region is considered as a positive example. Whereas, normal skin region and background pixels are treated as negative example. Partially overlapped Melanoma detected area is labeled using IoU threshold, below this threshold the region is considered as negative class region. The *IoU*

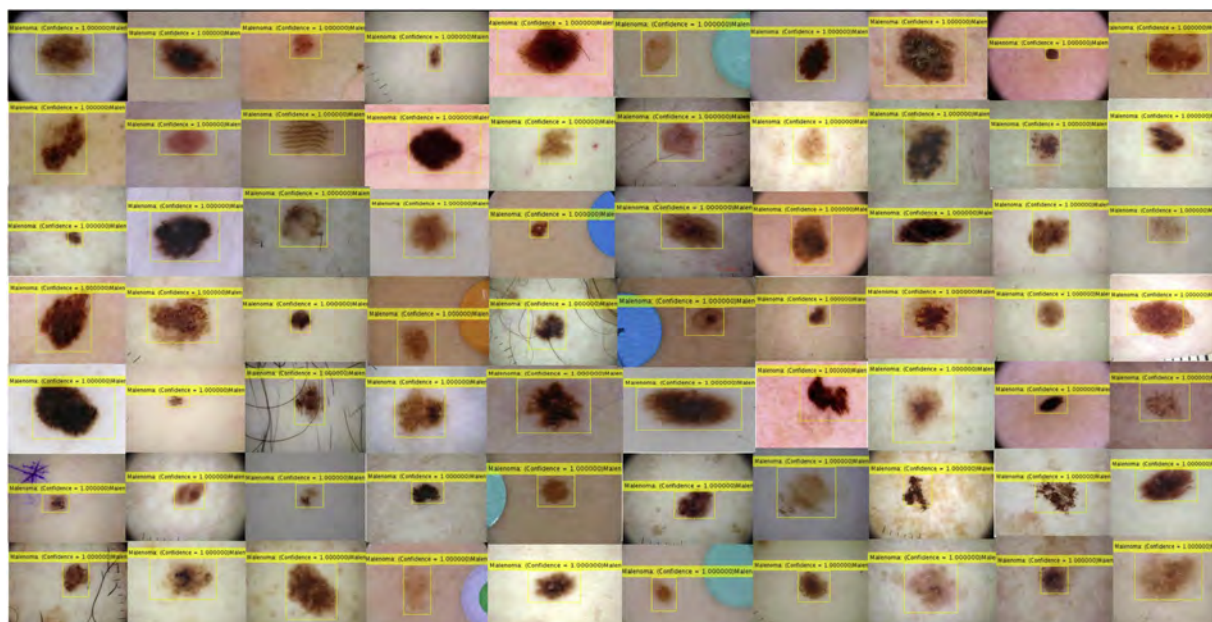


Fig. 5. 70 Test examples of high-scoring detections on the ISIC 2016 data set, selected from the top highest scoring Melanoma localization results.

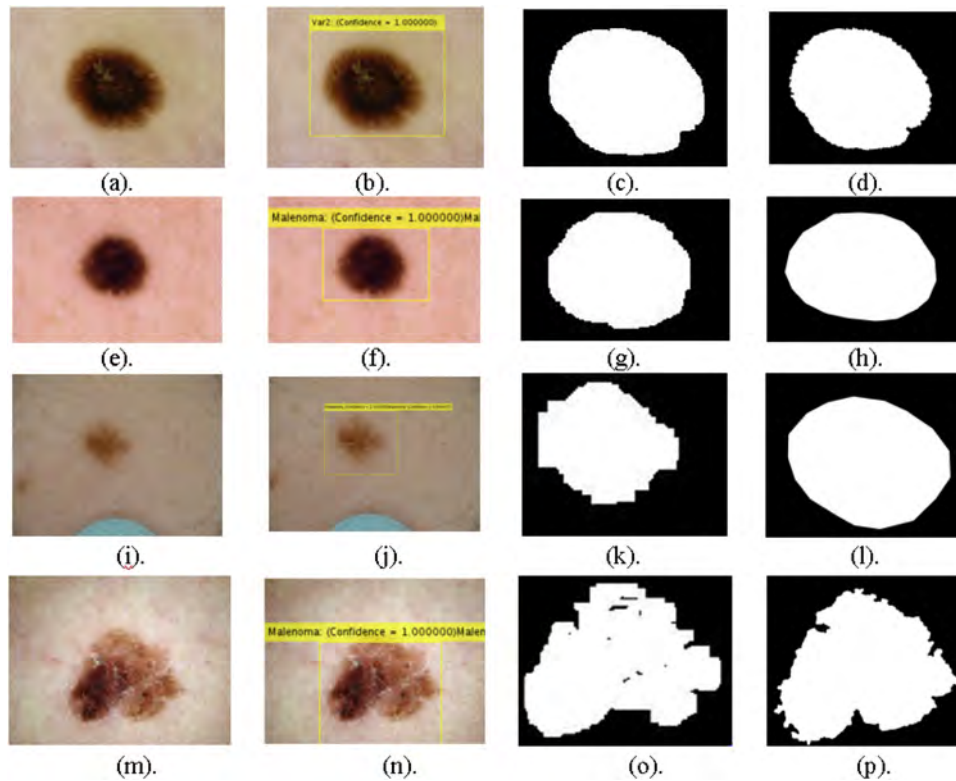


Fig. 6. (a), (e), (i) and (m) Input images with artifacts. (b), (f), (j) and (n) RCNN localization of Melanoma lesion. (c), (g), (k) and (o) Fuzzy segmentation of Melanoma boundary. (d), (h), (l) and (p) Ground truth Melanoma lesion images.

overlapping threshold chosen for Melanoma detection was 0.5. The IoU overlap greater than 0.5 detect the area as melanoma and IoU value lower than 0.3 detected as normal skin or black frame background region. The RCNN localized Melanoma region at regression layer with good *mAP* shown in Table 4. Some high scoring Melanoma detection results are presented in Fig. 5. From Fig. 5 it can be observe that RCNN localize the Melanoma area precisely, overcoming the artifacts of clinical swatches, clinical ruler marks, hair, and non-skin black frame pixels in background regions. Moreover, RCNN can detect Melanoma of different scale, orientation and at various location despite variation of skin color as shown in Fig. 5.

content

3.3.3. Melanoma segmentation

To compare the segmentation performance of detected Melanoma region, an accurate boundary area of Melanoma is required. The affected Melanoma boundary was obtained through FCM clustering algorithm. The algorithm grouped the Melanoma affected pixels in one cluster (Fig. 6c, g, k, o), whereas, all the remaining pixels are grouped separately. Therefore, the resultant segmented images are visually similar to the ground truth Melanoma images, as illustrated in Fig. 6(d, h, l, p).

Performance of the segmentation phase is evaluated by computing the *SP*, *SE*, *F1score*, *Ac*, at pixel-level for all images present in the test-set and the results are reported in Fig. 7. Proposed method achieved average values of *SP* as 0.9417, *SE* as 0.9781, *F1score* as 0.9589, *Ac* as 0.948. Similarly, *Di*, and *Jc* were computed for all test samples and average values were recorded. Average *Di* of segmentation was recorded as 0.94, which represent good segmentation performance. While, *Jc* averaged value on entire testing images was 0.93. The segmentation results are shown in Table 6 and compared with the state of the art methods, details are discussed in Section 3.5.1.

The reason behind the good performance of the proposed framework is an accurate localization of Melanoma region through RCNN.

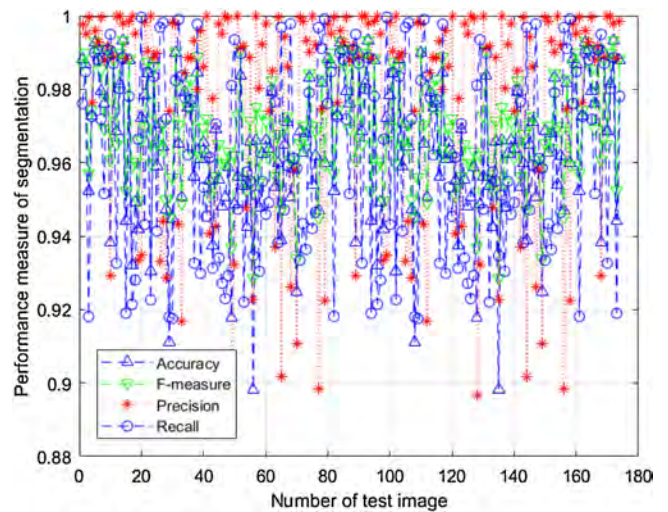


Fig. 7. Accuracy, F-measure, sensitivity, and specificity, on 175 test images are represented graphically.

However, in few images RCNN failed to precisely localize Melanoma due to visual similarity with normal skin, as shown in Fig. 8. In Fig. 7 the results over the test images are displayed graphically, portraying *SE* and *Ac* of few cases that are below 0.9, due to RCNN's erroneous prediction of normal skin pixels as Melanoma.

3.4. Comparative analysis

3.4.1. Comparisons over ISBI 2016 challenge

In ISBI 2016 challenge of skin lesion segmentation 28 teams reported results of their methods, the top ten teams results are represented in Table 5 [46]. All the participants were ranked according to

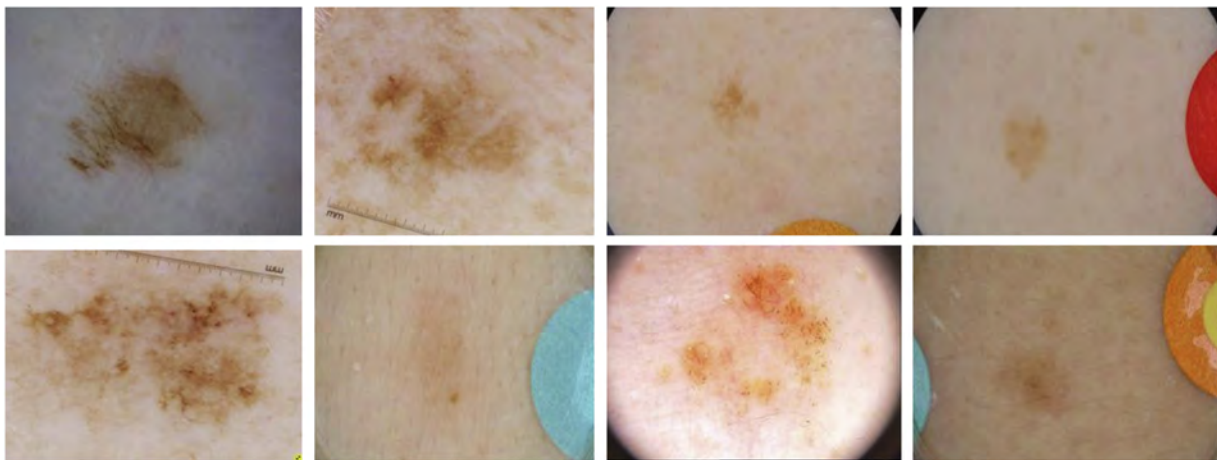


Fig. 8. RCNN failed to precisely localize Melanoma due to visual similarity with normal skin.

Table 5
Skin lesion segmentation results of ISBI 2016 challenge [46].

Method	AC	Di	Jc	SE	SP
ExB	0.95	0.91	0.84	0.91	0.965
CUMED	0.94	0.897	0.829	0.911	0.957
Mahmudur	0.952	0.895	0.822	0.88	0.969
SFU-mial	0.944	0.885	0.811	0.915	0.955
TMUteam	0.946	0.888	0.81	0.832	0.987
UiT-Seg	0.939	0.881	0.806	0.863	0.974
IHPC-CS	0.938	0.879	0.799	0.91	0.941
UNIST	0.94	0.867	0.797	0.876	0.954
Jose Luis	0.934	0.869	0.791	0.87	0.978
Marco romelli	0.936	0.864	0.786	0.883	0.962
Proposed	0.942	0.94	0.93	0.95	0.94

Table 6
Performance comparison.

Method	Ac	Di	Jc	SP	Time
Adaptive thresholding [19]	0.72	0.56	0.45	0.8	2
ISO [20]	0.82	0.68	0.56	0.77	–
Yen thresholding [21]	0.81	0.67	0.58	0.77	0.05
Level set active contour [22]	0.7	0.58	0.46	0.79	0.84
Statistical region growing [23]	0.73	0.55	0.43	0.76	0.4
Bootstrap learning [25]	0.78	0.72	0.57	0.75	–
Contextual hypergraph [24]	0.83	0.75	0.6	0.78	0.3
Sparse coding [26]	0.91	0.8	0.67	0.86	0.1
Segnet [35]	0.91	0.92	0.86	0.96	0.06
FCN [27]	0.82	0.82	0.86	0.70	0.05
Proposed method	0.94	0.94	0.93	0.942	0.08

the average value of Jc . The top ten participants used deep learning algorithm for segmentation due to effective performance gain over handcrafted features [33]. Majority of the participants at top ten position have used pre-trained models of CNN like Alexnet [49] and VGG [50], whereas we have used RCNN which has shallower network. Our proposed RCNN melanoma segmentation framework achieved Jc results better than all the participants. The top participant EXB [46] employed pre and post processing on images for precise segmentation. Whereas, second place winner participant CUMED [33] used fully convolutional residual network (FCRN) without pre and post processing with deep network.

To further examine the performance of the framework we have plotted box and whisker plot to understand the distribution of Jc performance metrics for all test images of our framework as compared to the state of the art methods (Fig. 9). The box and whisker plot representing the spread of Jc across the number line into four quartiles,

median, and outliers. Our resulting Jc represents smaller ratio of outliers and is comparable to top three participant, EXB [46], CUMED [33], and Mahmudur [46].

The spectrum Jc of the proposed methodology represents similar segmentation performance as compared to the challenge winners. Median Jc of our framework is at 0.83 which is fairly close to the median of boxplot of ExB [46]. Similarly, median Jaccard index Jc of [46] appears at 0.84, whereas [35] and [36] median Jc is at 0.86. Thus, preprocessing followed by RCNN and Fuzzy clustering algorithm significantly outperforms segmentation and localization of Melanoma, as compared to the state of the art techniques.

To estimate the performance of the proposed framework, we have plotted ROC curve as shown in Fig. 10. Our computed average value of the True Positive Rate (TPR) is (0.94) and the average False Positive Rate (FPR) is (0.057). Our ROC curve is higher than Mahmudur algorithm and closer to CuMed. It is notable from ROC Fig. 10 that our area under the curve represents good accuracy and cares about percentage of the relevant prediction results separating Melanoma area.

3.5. FCM evaluation

In this section we have compared the performance of the FCM clustering algorithm used in our paper against active contour segmentation method that is widely used in medical image segmentation research [19]. The results of the comparison over 50 randomly selected images are provided in Table 7. From the results it can be observed that the FCM has slightly improved segmentation results compare to the active contour method. Although the FCM explicitly demands the number of cluster centers whereas, this is not a requirement for the active contour method, but as we already have the precise information about the number of classes (i.e. melanoma affected and normal skin regions) therefore, the problem of grouping the data in wrong number of groups/classes never occurs.

3.5.1. Comparison with state-of-the-art techniques

The performance of our proposed framework has shown better segmentation results with respect to the state of the art methods, as shown in Table 6. Earlier studies for segmentation of affected skin region using basic segmentation techniques, such as thresholding [19–21], region merging [51,52], statistical region growing [23], clustering [53], active contour [22,54,55], bootstrap learning [25], contextual hypergraph [24], and sparse coding [26] with average Jc score of 0.54, which is lower than our method.

Deep learning based segmentation techniques such as FCN [27], and Segnet [35] performed segmentation with 0.86 Jc score. However, their network depth was deeper than our network, that makes the system

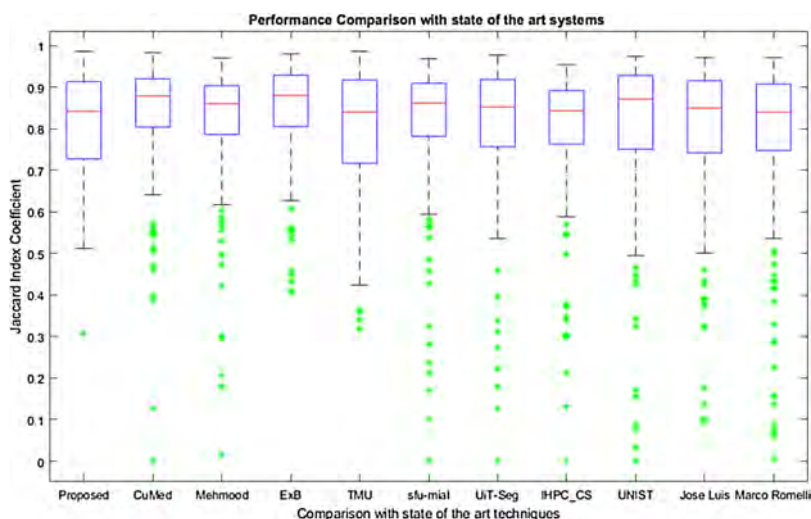


Fig. 9. Performance comparison with state of the art framework.

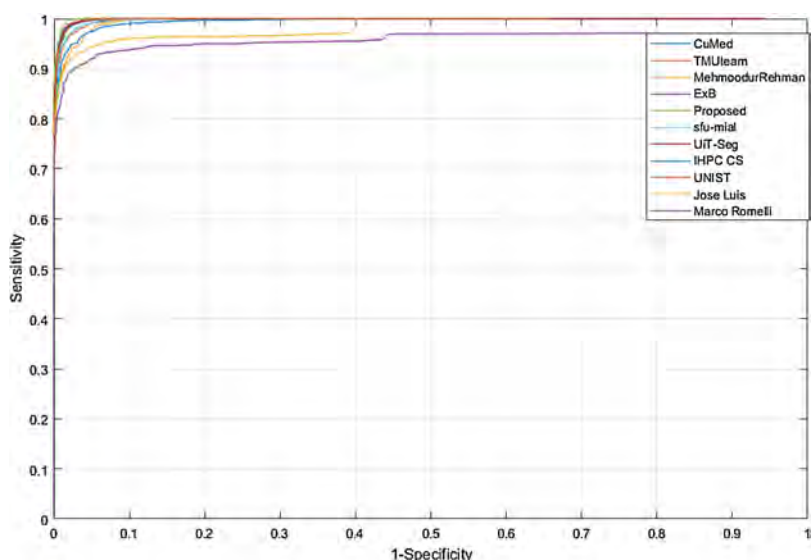


Fig. 10. Performance comparison with challenge winners.

Table 7

Comparing Melanoma segmentation performance of RCNN with FCM clustering and RCNN with Active contour method.

Method	Jc	Di	SE	SP
FCM	1.00	0.99	0.98	0.99
Active Contour	0.99	0.98	0.97	0.96

computational expensive in contrast with our method. From Table 6, it can be notable that our proposed method performed better than state of the art methods, due to good localization of Melanoma region using RCNN at shallower network with fewer computational resources. We have improved the segmentation results by 0.07 Jc score. According to Table 6, the computational time for traditional machine learning techniques is higher than our method, except the Yen's thresholding technique. The Yen's [21] thresholding technique is 1.6 times faster than our method, however, the segmentation performance in term of Ac, Jc, Di, SP are lower than our method. In contrast deep learning approach for segmentation, FCN [27] is 1.6 times faster than our method, where the segmentation performance is lower than our method.

4. Conclusion

In this paper, we proposed a novel a technique based on RCNN and FCM clustering for efficient precise and automated Melanoma region segmentation within dermoscopic images. Our method constitutes of three steps: skin refinement, localization of Melanoma region, and finally segmentation of Melanoma. In contrast with state of the art systems, the RCNN is capable to compute deep features with good representation of Melanoma, and hence improves the segmentation performance. The RCNN can detect multiple skin diseases of same patient as well as various diseases of different patients with efficient training mechanism and subject to sufficient training data. Moreover, our method can be applied to solve complex medical image segmentation problems. Series of experiments were performed on ISBI 2016 open source dataset “Skin Lesion Analysis towards Melanoma Detection”, validates the effectiveness of our method. Future research work in melanoma detection may include integration of classification task in the proposed method.

Authors' contributions

Nudrat Nida has designed and implemented the idea, and explore

the application of this technique in medical image analysis. Aun Irtaza performed simulations and integration of different phases of the methodology. He is also responsible for write-up of this paper. Aun Irtaza finalized the evaluation of different phases of the method. Ali Javed has finalized the methodology and experimented Fuzzy c means clustering for segmenting the precise boundary of Melanoma. Muhammad Haroon Yousaf has given the complete shape to this article and identified various aspects to be covered. His valuable feedback and technical support helped the primary author to overcome the challenges in dermoscopy images. M.T. Mahmood is responsible for proof reading along with technical support in different sections that includes skin refinement, removal of artifacts, detection of Melanoma and empirical analysis with state-of-the-art. All authors have read and approved the final manuscript.

Conflicts of interest

The authors declare no conflict of interest.

Summary Table

The contributions of our work are summarized as follows:

- Discriminating the melanoma regions from the normal skin regions through computer vision based segmentation is a challenging task. In this paper we utilized the RCNN based approach for melanoma detection. Our findings concludes that combination of RCNN with FCM results in precise detection of the affected regions, thus ensures the accurate recognition of the disease in an automatic way.
- RCNN was not previously used for medical analysis. Experimental analysis reveals capability of RCNN to identify Melanoma, acquiring deep, discriminative feature representation and obtaining better performance gain.
- The RCNN is also capable to detect multiple Melanoma regions in the input image; and if the patient suffers from various other skin diseases such as Lipoma, Fibroma, Sclerosis, Melanoma, etc. our system can detect these affected regions with higher precision. The characteristic of RCNN to detect multiple infectious area inspire more researchers to tap the potentials of RCNN to solve challenging problems of medical imaging analysis.
- Comparative analysis has demonstrated the superiority of the proposed method.

Acknowledgements

We gratefully acknowledge the support of NVIDIA Corporation with the donation of the Titan X Pascal GPU used for research work carried in Centre for Computer Vision Research (C²VR) at University of Engineering and Technology Taxila, Pakistan. This work was supported by Basic Science Research Program through the National Research Foundation of Korea (NRF) funded by the Ministry of Education (2016R1D1A1B03933860).

References

- [1] R.L. Siegel, K.D. Miller, S.A. Fedewa, D.J. Ahnen, R.G. Meester, A. Barzi, A. Jemal, Colorectal cancer statistics, 2017, CA: A Cancer J. Clin. 67 (2017) 177–193.
- [2] R.L. Siegel, K.D. Miller, A. Jemal, Cancer statistics, 2016, CA: A Cancer J. Clin. 66 (2016) 7–30.
- [3] F. Nachbar, W. Stolz, T. Merkle, A.B. Cognetta, T. Vogt, M. Landthaler, P. Bilek, O. Braun-Falco, G. Plewig, The ABCD rule of dermatoscopy: high prospective value in the diagnosis of doubtful melanocytic skin lesions, J. Am. Acad. Dermatol. 30 (1994) 551–559.
- [4] Z. Apalla, D. Nashed, R.B. Weller, X. Castellsagué, Skin cancer: epidemiology, disease burden, pathophysiology, diagnosis, and therapeutic approaches, Dermatol. Ther. 7 (2017) 5–19.
- [5] A. Esteva, B. Kuprel, R.A. Novoa, J. Ko, S.M. Swetter, H.M. Blau, S. Thrun, Dermatologist-level classification of skin cancer with deep neural networks, Nature 542 (2017) 115–118.

- [6] J. Burdick, O. Marques, A. Romero-Lopez, X. Giró Nieto, J. Weinthal, The impact of segmentation on the accuracy and sensitivity of a melanoma classifier based on skin lesion images, SIIM 2017 Scientific Program: Pittsburgh, PA, June 1–June 3, 2017, David L. Lawrence Convention Center (2017) 1–6.
- [7] S.A. Kostopoulos, P.A. Asvestas, I.K. Kalatzis, G.C. Sakellariopoulos, T.H. Sakkis, D.A. Cavouras, D.T. Glotsos, Adaptable pattern recognition system for discriminating melanocytic nevi from malignant melanomas using plain photography images from different image databases, Int. J. Med. Inform. 105 (2017) 1–10.
- [8] E. Okur, M. Turkan, A survey on automated melanoma detection, Eng. Appl. Artif. Intell. 73 (2018) 50–67.
- [9] R.J. Stanley, W.V. Stoecker, R.H. Moss, A relative color approach to color discrimination for malignant melanoma detection in dermoscopy images, Skin Res. Technol. 13 (2007) 62–72.
- [10] N.K. Mishra, M.E. Celebi, An overview of melanoma detection in dermoscopy images using image processing and machine learning, (2016) arXiv preprint. arXiv:1601.07843.
- [11] Y.I. Cheng, R. Swamisai, S.E. Umbaugh, R.H. Moss, W.V. Stoecker, S. Teegala, S.K. Srinivasan, Skin lesion classification using relative color features, Skin Res. Technol. 14 (2008) 53–64.
- [12] L. Ballerini, R.B. Fisher, B. Aldridge, J. Rees, A color and texture based hierarchical k-NN approach to the classification of non-melanoma skin lesions, Color Medical Image Analysis, Springer, 2013, pp. 63–86.
- [13] C. Barata, M.E. Celebi, J.S. Marques, Development of a clinically oriented system for melanoma diagnosis, Pattern Recognit. 69 (2017) 270–285.
- [14] R. Garnavi, M. Aldeen, M.E. Celebi, A. Bhuiyan, C. Dolianitis, G. Varigos, Automatic segmentation of dermoscopy images using histogram thresholding on optimal color channels, Int. J. Med. Med. Sci. 1 (2010) 126–134.
- [15] T. Tommasi, E. La Torre, B. Caputo, Melanoma recognition using representative and discriminative kernel classifiers, International Workshop on Computer Vision Approaches to Medical Image Analysis, Springer (2006) 1–12.
- [16] H. Ganster, P. Pinz, R. Rohrer, E. Wildling, M. Binder, H. Kittler, Automated melanoma recognition, IEEE Trans. Med. Imaging 20 (2001) 233–239.
- [17] M.E. Celebi, H.A. Kingravi, B. Uddin, H. Iyatomi, Y.A. Aslandogan, W.V. Stoecker, R.H. Moss, A methodological approach to the classification of dermoscopy images, Comput. Med. Imaging Graph. 31 (2007) 362–373.
- [18] G. Schaefer, B. Krawczyk, M.E. Celebi, H. Iyatomi, An ensemble classification approach for melanoma diagnosis, Memet. Comput. 6 (2014) 233–240.
- [19] M. Silveira, J.C. Nascimento, J.S. Marques, A.R. Marçal, T. Mendonça, S. Yamauchi, J. Maeda, J. Rozeira, Comparison of segmentation methods for melanoma diagnosis in dermoscopy images, IEEE J. Sel. Top. Signal Process. 3 (2009) 35–45.
- [20] T. Ridler, S. Calvard, et al., Picture thresholding using an iterative selection method, IEEE Trans. Syst. Man Cybern. 8 (1978) 630–632.
- [21] M. Sezgin, B. Sankur, Survey over image thresholding techniques and quantitative performance evaluation, J. Electron. Imaging 13 (2004) 146–166.
- [22] C. Li, C.-Y. Kao, J.C. Gore, Z. Ding, Minimization of region-scalable fitting energy for image segmentation, IEEE Trans. Image Process. 17 (2008) 1940–1949.
- [23] M. Emre Celebi, H.A. Kingravi, H. Iyatomi, Y. Alp Aslandogan, W.V. Stoecker, R.H. Moss, J.M. Malters, J.M. Grichnik, A.A. Marghoob, H.S. Rabinovitz, et al., Border detection in dermoscopy images using statistical region merging, Skin Res. Technol. 14 (2008) 347–353.
- [24] X. Li, Y. Li, C. Shen, A. Dick, A. Van Den Hengel, Contextual hypergraph modeling for salient object detection, Computer Vision (ICCV), 2013 IEEE International Conference on, IEEE (2013) 3328–3335.
- [25] N. Tong, H. Lu, X. Ruan, M.-H. Yang, Salient object detection via bootstrap learning, Computer Vision and Pattern Recognition (CVPR), 2015 IEEE Conference on, IEEE (2015) 1884–1892.
- [26] B. Bozorgtabar, M. Abedini, R. Garnavi, Sparse coding based skin lesion segmentation using dynamic rule-based refinement, International Workshop on Machine Learning in Medical Imaging, Springer (2016) 254–261.
- [27] J. Long, E. Shelhamer, T. Darrell, Fully convolutional networks for semantic segmentation, Proceedings of the IEEE Conference on Computer Vision and Pattern Recognition (2014) 3431–3440.
- [28] N. Tajbakhsh, J.Y. Shin, S.R. Gurudu, R.T. Hurst, C.B. Kendall, M.B. Gotway, J. Liang, Convolutional neural networks for medical image analysis: full training or fine tuning? IEEE Trans. Med. Imaging 35 (2016) 1299–1312.
- [29] A.A.A. Setio, F. Ciompi, G. Litjens, P. Gerke, C. Jacobs, S.J. van Riel, M.M.W. Wille, M. Naqibullah, C.I. Sánchez, B. van Ginneken, Pulmonary nodule detection in ct images: false positive reduction using multi-view convolutional networks, IEEE Trans. Med. Imaging 35 (2016) 1160–1169.
- [30] M. Anthimopoulos, S. Christodoulidis, L. Ebner, A. Christe, S. Mougkakakou, Lung pattern classification for interstitial lung diseases using a deep convolutional neural network, IEEE Trans. Med. Imaging 35 (2016) 1207–1216.
- [31] H.-C. Shin, H.R. Roth, M. Gao, L. Lu, Z. Xu, I. Nogues, J. Yao, D. Mollura, R.M. Summers, Deep convolutional neural networks for computer-aided detection: CNN architectures, dataset characteristics and transfer learning, IEEE Trans. Med. Imaging 35 (2016) 1285–1298.
- [32] W.O. Nijeweme-d'Hollosy, L. van Velsen, M. Poel, C.G. Groothuis-Oudshoorn, R. Soer, H. Hermens, Evaluation of three machine learning models for self-referral decision support on low back pain in primary care, Int. J. Med. Inform. 110 (2018) 31–41.
- [33] L. Yu, H. Chen, Q. Dou, J. Qin, P.-A. Heng, Automated melanoma recognition in dermoscopy images via very deep residual networks, IEEE Trans. Med. Imaging 36 (2017) 994–1004.
- [34] M. Attia, M. Hossny, S. Nahavandi, A. Yazdabadi, Skin melanoma segmentation using recurrent and convolutional neural networks, Biomedical Imaging (ISBI 2017), 2017 IEEE 14th International Symposium on, IEEE (2017) 292–296.

- [35] V. Badrinarayanan, A. Handa, R. Cipolla, Segnet: a deep convolutional encoder-decoder architecture for robust semantic pixel-wise labelling, (2015) arXiv preprint. [arXiv:1505.07293](https://arxiv.org/abs/1505.07293).
- [36] L. Bi, J. Kim, E. Ahn, D. Feng, M. Fulham, Semi-automatic skin lesion segmentation via fully convolutional networks, ISBI (2017).
- [37] R. Girshick, J. Donahue, T. Darrell, J. Malik, Region-based convolutional networks for accurate object detection and segmentation, IEEE Trans. Pattern Anal. Mach. Intell. 38 (2016) 142–158.
- [38] A. Polesel, G. Ramponi, V.J. Mathews, Image enhancement via adaptive unsharp masking, IEEE Trans. Image Process. 9 (2000) 505–510.
- [39] L.-h. Xu, Z.-s. Chen, Region labeling based on run-length coding for binary image, Opto-electron. Eng. 6 (2004).
- [40] J.R. Uijlings, K.E. Van De Sande, T. Gevers, A.W. Smeulders, Selective search for object recognition, Int. J. Comput. Vis. 104 (2013) 154–171.
- [41] P. Viola, M. Jones, Rapid object detection using a boosted cascade of simple features, Computer Vision and Pattern Recognition, 2001. CVPR 2001. Proceedings of the 2001 IEEE Computer Society Conference on, vol. 1, IEEE (2001) pp. I-I.
- [42] N. Dalal, B. Triggs, Histograms of oriented gradients for human detection, Computer Vision and Pattern Recognition, 2005. CVPR 2005. IEEE Computer Society Conference on, vol. 1, IEEE (2005) 886–893.
- [43] A. Krizhevsky, V. Nair, G. Hinton, The cifar-10 Dataset, (2014) <http://www.cs.toronto.edu/kriz/cifar.html>.
- [44] J. Yosinski, J. Clune, Y. Bengio, H. Lipson, How transferable are features in deep neural networks? Advances in Neural Information Processing Systems (2014) 3320–3328.
- [45] W. Cai, S. Chen, D. Zhang, Fast and robust fuzzy c-means clustering algorithms incorporating local information for image segmentation, Pattern Recognit. 40 (2007) 825–838.
- [46] D. Gutman, N.C. Codella, E. Celebi, B. Helba, M. Marchetti, N. Mishra, A. Halpern, Skin Lesion Analysis Toward Melanoma Detection: A Challenge at the International Symposium on Biomedical Imaging (ISBI) 2016, Hosted by the International Skin Imaging Collaboration (ISIC), (2016) arXiv preprint. [arXiv:1605.01397](https://arxiv.org/abs/1605.01397).
- [47] Z. Wang, A.C. Bovik, Mean squared error: love it or leave it? A new look at signal fidelity measures, IEEE Signal Process. Mag. 26 (2009) 98–117.
- [48] Z. Wang, A.C. Bovik, L. Lu, Why is image quality assessment so difficult? Acoustics, Speech, and Signal Processing (ICASSP), 2002 IEEE International Conference on, vol. 4, IEEE (2002) pp. IV-3313.
- [49] A. Krizhevsky, I. Sutskever, G.E. Hinton, Imagenet classification with deep convolutional neural networks, Advances in Neural Information Processing Systems (2012) 1097–1105.
- [50] K. Simonyan, A. Zisserman, Very deep convolutional networks for large-scale image recognition, (2014) arXiv preprint. [arXiv:1409.1556](https://arxiv.org/abs/1409.1556).
- [51] A. Wong, J. Scharcanski, P. Fieguth, Automatic skin lesion segmentation via iterative stochastic region merging, IEEE Trans. Inf. Technol. Biomed. 15 (2011) 929–936.
- [52] H. Castillejos, V. Ponomaryov, L. Nino-de Rivera, V. Golikov, Wavelet transform fuzzy algorithms for dermoscopic image segmentation, Comput. Math. Methods Med. 2012 (2012).
- [53] Z. Liu, J. Zerubia, Skin image illumination modeling and chromophore identification for melanoma diagnosis, Phys. Med. Biol. 60 (2015) 3415.
- [54] R.B. Oliveira, N. Marranghello, A.S. Pereira, J.M.R. Tavares, A computational approach for detecting pigmented skin lesions in macroscopic images, Expert Syst. Appl. 61 (2016) 53–63.
- [55] H. Zhou, X. Li, G. Schaefer, M.E. Celebi, P. Miller, Mean shift based gradient vector flow for image segmentation, Comput. Vis. Image Underst. 117 (2013) 1004–1016.